eNeuro

Research Article: New Research | Disorders of the Nervous System

Functional mechanisms of recovery after chronic stroke: modeling with The Virtual Brain,,

The Virtual Brain models stroke recovery processes

Maria Inez Falcon[1], Jeffrey D. Riley[1], Viktor Jirsa[2,3], Anthony R McIntosh[4], E Elinor Chen[1] and Ana Solodkin[1,5]

[1]*Department of Anatomy and Neurobiology. UC Irvine School of Medicine. Irvine, CA 92697, USA*

[2]*Institut de Neurosciences des Systèmes - Aix-Marseille Université - Faculté de Médecine, Marseille F-13000, France*

[3]*Inserm UMR1106, Marseille F-13000, France*

[4]*Rotman Research Institute, Baycrest Health Sciences, M6A 2E1 University of Toronto, Toronto, Canada*

[5]*Department of Neurology. UC Irvine School of Medicine. Irvine, CA 92697, USA*

Address correspondence to: Ana Solodkin, PhD, Anatomy and Neurobiology; Neurology, Hewett Hall, Room 1505, UC Irvine Medical School, Irvine, CA 92697, E-mail: Solodkin@uci.edu

Alerts: Sign up at eneuro.org/alerts to receive customized email alerts when the fully formatted version of this article is published.

eNeuro

eN-NWR-0158-15R1

Functional mechanisms of recovery after chronic stroke: modeling with The Virtual Brain

Functional mechanisms of recovery after chronic stroke: modeling with *The Virtual Brain*

Abbreviated Title: The Virtual Brain models stroke recovery processes

Maria Inez Falcon [1]; Jeffrey D. Riley[1]; Viktor Jirsa[2,4]; Anthony R McIntosh[5]; E Elinor Chen[1]; and Ana Solodkin[1,3]

1. Department of Anatomy and Neurobiology. UC Irvine School of Medicine. Irvine, CA. 92697. USA **2.** Institut de Neurosciences des Systèmes - Aix-Marseille Université - Faculté de Médecine, Marseille, F-13000, France. **3.** Department of Neurology. UC Irvine School of Medicine. Irvine, CA. 92697. USA **4.** Inserm UMR1106 – Marseille F-13000, France; **5.** Rotman Research Institute, Baycrest Health Sciences, M6A 2E1 University of Toronto, Toronto, Canada.

Author Contributions

All authors had full access to all data in the study and take responsibility for the integrity of the data and the accuracy of the data analysis. AS, VJ, and MIF Designed Research; AS, JR and MIF Performed research; AS, MIF, JR, VJ, EEC, and ARM Analyzed data; MIF, AS, VJ, JR, and ARM Wrote the paper

Address correspondence to:
Ana Solodkin, PhD
Anatomy and Neurobiology; Neurology
Hewett Hall, Room 1505
UC Irvine Medical School
Irvine CA, 92697
Solodkin@uci.edu

Nuumber of Figures: 6
Number of Tables: 3
Number of Multimedia: 0
Number of Words for Abstract: 250
Number of Words for Significance Statement: 115
Number of Words in Introduction: 666

37　**Number of Words in Discussion:** 2159

38

39　**Acknowledgments**

45

46　The authors report no conflict of interest.

47

Abstract

49

50 　　We have seen important strides in our understanding of mechanisms underlying stroke

51 recovery, yet effective translational links between basic and applied sciences, as well as from

52 big data to individualized therapies, are needed to truly develop a cure for stroke. We present

53 such an approach using The Virtual Brain (TVB), a neuroinformatics platform that employs

54 empirical neuroimaging data to create dynamic models of an individual's human brain;

55 specifically, we simulate fMRI signals by modeling parameters associated with brain dynamics

56 after stroke.

57 　　In twenty individuals with stroke and 11 controls we obtained rest fMRI, T1w, and DTI

58 data. Motor performance was assessed pre-therapy, post-therapy, and 6-12 months post-

59 therapy. Based on *individual* structural connectomes derived from DTI, the following steps

60 were performed in the TVB platform: 1) Optimization of local and global parameters

61 (conduction velocity, global coupling), 2) Simulation of BOLD signal using optimized

62 parameter values, 3) Validation of simulated time series by comparing frequency, amplitude,

63 and phase of the simulated signal with empirical time series, 4) Multivariate linear regression

64 of model parameters with clinical phenotype.

65 　　Compared to controls, individuals with stroke demonstrated a consistent reduction in

66 conduction velocity, increased local dynamics, and reduced local inhibitory coupling. A

67 negative relationship between local excitation and motor recovery, and a positive correlation

68 between local dynamics and motor recovery were seen.

69 　　TVB reveals a disrupted post-stroke system favoring excitation-over-inhibition and

70 local-over-global dynamics, consistent with existing mammal literature on stroke mechanisms.

71   Our results point to the potential of TVB to determine individualized biomarkers of stroke

72   recovery.

73

74   **Significance Statement**

75   The development of schemes to acquire neuroimaging big data is fostering a greater

76   understanding of brain function. Yet we are lacking quantitative tools to translate these insights

77   to the individual level, particularly associated with neurological disease. We address this

78   challenge using the neuroinformatics platform, *The Virtual Brain*, to model individualized

79   brain activity. This approach enables the linkage of macroscopic brain dynamics with

80   mesoscopic biophysical parameters, wherein we demonstrate the capacity of large-scale brain

81   models to track and predict long-term recovery after stroke. Our results establish the basis for

82   a deliberate integration of computational biology and neuroscience into clinical approaches for

83   elucidating cellular mechanisms of disease, opening new venues for the development of

84   individualized therapeutic interventions.

85

Introduction

86

87   Previous research has provided key insights into the disease process in stroke. Studies

88 in mammals have uncovered basic mechanisms of ischemic injury, inflammatory responses,

89 and cellular recovery (Carmichael, 2012; Nudo, 2013). In humans, researchers have suggested

90 predictive imaging biomarkers for disease progression and recovery, mapped associated

91 changes in brain networks, and developed new rehabilitative therapies (Reiss et al., 2012).

92 Despite this, stroke remains a major source of disability in the United States, with

93 approximately 6.5 million people living with stroke, with some level of hemiparesis present in

94 approximately 50% (Go et al., 2014). This is neither the fault of mammal nor human studies,

95 as both are constrained by their respective study populations. Studies in mammals are well-

96 controlled yet homogeneous, limiting their translational abilities. Human studies reflect the

97 population at hand, yet often rely on indirect measures, obscuring the full picture. Although

98 both share a common goal of curing stroke via the repair and reorganization of the injured

99 brain, what is missing is a translational bridge to effectively span the divide between basic

100 mechanisms and dynamic human brain systems.

101   At the same time, the neuroscience community is immersed in collecting large datasets

102 to provide greater understanding of brain function and dysfunction. Such initiatives span

103 normal function (Human Connectome Project), development (NIH Pediatric Database), and

104 brain disorders such as Alzheimer's disease (ADNI) and mental illness (Research Domain

105 Criteria Project). While these initiatives provide the necessary empirical foundation,

106 quantitative tools are missing to integrate these multiple datasets to "reconstruct" the brain,

107 and provide the link between these data and those from a single person.

108   Over the last 6 years, a neuroinformatics platform has been developed: The Virtual

109   Brain (TVB) (Sanz Leon et al., 2013). The defining feature of TVB is that it generates

110   *personalized* functional neuroimaging data based on individual structural connectome data to

111   create personalized virtual brains. These models are specific to each individual person, and

112   contain the connectivity between parts of the brain and the dynamics of local neural

113   populations. TVB uses structural MRI data to create the custom brain surface, diffusion-

114   weighted MRI data to infer the anatomical connections between brain areas, and then

115   functional MRI data as the target to modify the parameters of the model to reproduce the

116   observed functional data. The neuroinformatics architecture of TVB houses a library of

117   models, which catalogues the biophysical parameters that produce different empirical brain

118   states (Ritter et al., 2013). Global biophysical parameters represent biological mechanisms

119   governing dynamics between brain regions, while the local biophysical parameters describe

120   the properties of small populations of neurons integrating dynamics at the local mesoscopic

121   level. That is, modeling in TVB comprises multiple scales of brain dynamics that are invisible

122   to brain imaging devices, and therefore TVB acts as a "computational microscope," allowing

123   the inference of internal states and processes of the system.

124   TVB thus offers a novel platform to formulate biologically interpretable hypotheses on

125   the effects of stroke and its recovery based on biophysical mechanisms governing brain

126   dynamics. Beyond the direct clinical implications of network dysfunction in stroke, these

127   insights can contribute a first step to the understanding of fundamental mechanisms of the

128   brain's structure-function relationship. TVB has been established and applied to normative

129   data sets (Deco et al., 2012) and for learning and plasticity (Roy et al., 2014), yet a proof of

130   concept needs to be established based on pathological states.

131   The objective of the present study using the TVB platform was to determine changes

132   in local and global biophysical parameters to better understand individualized brain dynamics

133   after stroke. In this approach, the model parameters act as a means to assess brain health,

134   analogous to blood samples assessing physical health, and hence, parameter changes could

135   ideally be used as potential biomarkers of stroke and/or stroke recovery. So far, such

136   biomarkers have mostly focused on stable architectures, from behavior to fine anatomical and

137   functional levels (Burke and Cramer, 2013). In contrast, our aim is to create a synergistic

138   amalgamation of mathematical models with neuroimaging, where the biomarker derives from

139   the dynamical model itself.

140   **Methods**

141   *Subjects:*

142   Twenty volunteers with chronic stroke (ages 23-74, 8 females) in the middle cerebral

143   artery (MCA) territory and 11 age-matched controls were included in the study. Human

144   subjects were recruited at a location that will be identified if the article is published.

145   Demographic details and stroke characteristics of our cohort can be found in **Table 1**.

146   Motor performance was assessed with: the Functional Ability Scale of the Wolf Motor

147   Function Test (WMFT), Nine-hole peg test, the Fugl-Meyer upper arm test, and the Motor

148   Activity Log (MAL-14). These assessments were collected at baseline (pre-therapy), after one

149   month of intensive hand therapy (post-therapy) and 6-12 months after therapy (maintenance).

150

151   *Brain Imaging:*

152   Imaging data were acquired on a 3 Tesla Philips Achieva scanner using the following

153   sequences:

154   **1.** High-resolution anatomical images were acquired with a 3D Magnetization

155   Prepared Rapid Gradient Echo (MP-RAGE) sequence: FOV= 250x250,

156   resolution=1x1x1mm, SENSE reduction factor =1.5, TR/TE=7.4/3.4ms, flip

157   angle=8, sagittal orientation, number of slices=301 covering the whole brain.

158   **2.** Diffusion Tensor Imaging was acquired with the following sequence:

159   FOV=224x224, TR/TE=13030/55, 72 slices, slice thickness= 2mm,

160   resolution=0.875x0.875x2, 2 mm post-processing iso-voxel with b=1000 sec/mm^2

161   (and b=0), 32 diffusion directions.

162   **3.** Functional imaging acquisition at rest covering the whole brain (37 slices) was

163   acquired using single-shot echo-planar MR (EPI) with slice thickness = 4.0 mm,

164   FOV= 230x230, voxel size = 2.8mm x 2.8mm, TR/TE= 2000/20 ms, duration= 5

165   min.

166   *Virtual Brain Transplantation:*

167   Because of mechanical deformation consequent to large cortical strokes, the anatomical

168   parcellation on T1w images using semi-automated methods is very difficult to achieve.

169   Hence, a "virtual brain transplant" process was performed in accordance with a

170   previous approach (Solodkin et al., 2010). This method replaces the cortical lesion with

171   the homologous image from the contralesional hemisphere from the same subject. With

172   this, brain parcellation is possible using semi-automatized software. The process

173   consisted of the following steps:

174   **1.** Lesion segmentation by hand.

175   **2.** Using the AFNI 3dcalc function (Cox, 1996), the homologous region in the non-

176   lesioned hemisphere was dissected and transplanted into the stroke region,

8

177   effectively filling in the missing portions of the brain.

178   **3.** Manual corrections were then done in the interface between the native and

179   transplanted T1-w images by visually examining each voxel and making voxel

180   intensities uniform using AFNI's 3dLocalStat and 3dcalc commands.

181   **4.** The brain was then parcellated into 96 cortical and subcortical regions. The original

182   parcellation based on a macaque template (Van Essen, 2004) was transformed to

183   the human MNI template via PALS (Van Essen, 2005). To increase accuracy, the

184   deformation process was carried out using landmarks (based on CARET) and

185   functional activation patterns considered homologous between the two species

186   (Van Essen and Dierker, 2007).

187

188   *Diffusion Tensor Imaging:*

189   Pre-processing of DTI data consisted of 1) motion correction using the FSL eddy

190   current correction (Leemans and Jones, 2009), 2) generation of a binary brain mask from the

191   b0 image and application of the mask to all diffusion images using the Brain Extraction Tool

192   from FSL (Smith, 2002), 3) fitting of a diffusion tensor at each voxel using FSL's dtifit

193   function, 4) non-linear co-registration of T1 data to the MNI brain and co-registration of T1

194   images to their respective DTI images producing an MNI to DTI transformation using ANTS

195   (Avants et al., 2011), 5) white and gray matter segmentation performed on the MNI-to-T1 atlas

196   using FAST (Zhang et al., 2001) and 6) parcellation of the gray matter into 96 regions as

197   described above and registration of these regions to the DTI using the T1-to-DTI

198   transformation with a nearest neighbor interpolation.

199

9

Tractography and Structural Connectivity Matrix Generation

200

201   **1.** Probabilistic tractography was performed to trace the fiber bundles associated with

202   pairs of cortical regions in the MNI space, which were defined as edges in the

203   network (Ritter et al., 2013; Zalesky and Fornito, 2009).

204   **2.** Two connectivity measures were extracted: a) capacities, depicting the maximum

205   rate of transmission of information through edges, were calculated using the

206   number of streamlines at the minimum cross-sectional area of an edge (Zalesky and

207   Fornito, 2009); and b) distances, defined by the lengths of each edge, were

208   calculated by averaging the lengths of all streamlines in an edge. These measures

209   were used to generate two 96x96 structural connectivity matrices. Quality

210   assurance to reduce false positives was performed on each structural connectivity

211   matrix by a trained neuroanatomist (AS).

212

213   *Resting State fMRI Pre-processing*

214   Pre-processing was done in AFNI (Cox, 1996) and included the following steps: motion

215   correction of functional and anatomical data sets (Cox and Jesmanowicz, 1999), 3D spatial

216   registration to a reference acquisition from the rsfMRI run, registration of functional images

217   to the T1-w volume, despiking and mean normalization of the time series, motion correction

218   (>1mm, (Johnstone et al., 2006)) and regression of cerebrospinal fluid and white matter

219   signals to remove slow-wave components (e.g. physiological noise) (Lund et al., 2006).

220

221   *Resting State fMRI Post-processing*

222   Average time series were extracted for each of 96 MNI regions. For each subject, a

223   96x96 functional connectivity matrix was generated by calculating the pair-wise correlation

224   of the time series for each region (Ritter et al., 2013) using the "corr" function in Matlab.

225

226   *Modeling in TVB (Figure 1):*

227   The Virtual Brain (TVB version 1.08) was used for all simulations (Sanz Leon et al.,

228   2013) where the principal empirical input to the platform is the structural connectivity matrix

229   derived from each individual subject's tractography. Based on this input, TVB simulates field

230   potentials by integrating global dynamics with a local (mesoscopic) model that determines

231   the dynamics *within* brain regions. Following, BOLD signals are derived from the generated

232   field potentials. In this work, we used the Stefanescu-Jirsa 3D (SJ3D, Figure 2) local model,

233   as the resulting mean field model does not rely heavily on synaptic delays (Jirsa and

234   Stefanescu, 2011; Sanz-Leon et al., 2015; Stefanescu and Jirsa, 2008), making it compatible

235   with the poor time resolution associated with BOLD signals. Specifically, the SJ3D model is

236   derived from populations of bursting neurons and includes six states describing excitatory and

237   inhibitory dynamics via the inclusion of a variety of biophysical parameters defining the local

238   mean fields (for a list of the parameter values used in the present study see Table 2)

239   (Hindmarsh and Rose, 1984; Stefanescu and Jirsa, 2008).

240   The following sequential steps were performed for each individual subject:

241   1)   Importing of a subject-specific connectivity matrix into the TVB platform.

242   2)   Selection of the SJ3D local model.

243   3)   Parameter Space Estimation (exploration and fitting): We sequentially

244   performed systematic parameter space explorations and fitting to determine the optimal values

11

245   for global and local parameters in all subjects. a) Parameter space exploration: We used heat

246   maps of global variance (mean variance of time series across all brain regions) to constrain the

247   range of values for each model parameter (Figure 3). The range of values considered is assessed

248   based on those values with high global variance flanked by bifurcation points (Breakspear and

249   Jirsa, 2007). An additional advantage of this approach is that it is not only pragmatic but it can

250   also provide information on the degree of variability and sensitivity that parameter values have

251   onto the simulated signals. b) Parameter fitting: The final optimal value was subsequently

252   obtained by assessing the specific value for the parameters that resulted in the best fit between

253   the empirical and simulated signals based on three metrics described below (step 6). The global

254   parameters explored included conduction velocity and global coupling and the local parameters

255   included K_{12} (excitatory on inhibitory coupling), K_{21} (inhibitory on excitatory coupling), and

256   K_{11} (excitatory on excitatory coupling). The local parameters were chosen as they have the

257   strongest impact on the dynamics of the SJ3D model (Stefanescu and Jirsa, 2008).

258   4)   Stochastic Network simulation: Based on the values obtained in the parameter

259   space exploration, we generated field potentials with the same duration (4 min) and sampling

260   rate (TR=2s) as the empirical rsfMRI acquisition. The length of the simulated data was kept

261   equal to the length of the empirical data in order to minimize the influence of variability over

262   the course of the time series, as it is becoming increasingly patent that values of functional

263   connectivity are not stable over time (Hutchison et al., 2013). White noise with Gaussian

264   amplitude (mean = 0, standard deviation = 1) was added to each node. Numerical integration

265   of the system was performed using stochastic Heun's method (Mannella 2002), with an

266   integration step size of 0.0122 ms.

267   5)   The BOLD signals were derived from the field potentials using a

268   haemodynamic response function implemented with a gamma kernel (Boynton et al., 1996;

269   Sanz-Leon et al., 2015).

270   6)   Assessing reliability of the simulated time series: Comparison between the

271   empirical and simulated BOLD time series was done in terms of amplitude, frequency, and

272   phase.

273   Amplitude: We calculated the range of amplitude by identifying the highest and lowest

274   peaks present in the time series across all regions.

275   Frequency: Fast Fourier transforms of the raw and simulated time series were obtained

276   using Matlab's "fft" function with a sampling frequency of 0.5 hz, to determine the range,

277   profile, and peak frequencies (Ritter et al., 2013).

278   Phase: This was assessed by comparing the functional connectivity matrices of the

279   simulated and empirical time series. We averaged all matrices from healthy controls to obtain

280   a group control matrix, and calculated the pairwise linear correlation coefficient between the

281   simulated functional connectivity matrix for each individual to the group.

282   7)   Differences in parameter values between healthy controls and stroke cases were

283   evaluated with Wilcoxon sum rank test corrected for multiple comparisons (Bonferroni).

284   8)   Relationship with clinical phenotype

285   In order to determine if there was any relationship between TVB parameters and the

286   clinical phenotype, multiple linear regression was performed between model parameters

287   (dependent variables) and the following independent variables: Motor outcome measures

288   (Fugl-Meyer, WMFT, 9-hole peg and MAL-14), patient demographics (age, sex, presence of

289   depression) and lesion characteristics (size, location, time after stroke, side of stroke).

290

291 **Results**

292

293 *Weights of structural connections after stroke*

294 The weights of connections in the control group had a mean ($\pm$ SD) of 10.16 ± 1.03,

295 (range 8.75-12.07), and in the stroke cohort had a mean of 9.76 ± 1.57 (range 6.41-10.35)

296 (Figure 4). Yet, there were no statistical differences in mean, distribution shape between the

297 groups (Kolmogorov-Smirnov test; $p_a = 0.42$), or skewness (controls = -0.083; stroke = -0.082;

298 t-test: p=0.35 and 0.29 respectively).

299

300 *BOLD simulations generated with TVB correlated with the empirical BOLD*

301 *responses (Figure 5)*

302 The frequency spectrums of the simulated and the empirical BOLD responses had

303 similar ranges (0-0.25 Hz) and mean peak (empirical = 0.05+0.035 Hz; simulated = 0.03+0.023

304 Hz). Although the mean amplitudes were similar (empirical = 8.15; simulated = 9.49), the

305 range of values was wider in the empirical signals (0.17 – 87.43) than those found in the

306 simulated BOLD (3.79 – 22.64). The relative phases of the regions within simulated and

307 empirical time series were similar as assessed by the mean correlation coefficient between their

308 respective functional connectivity matrices (mean = 0.27 ± 0.02; p_b = 0. 9e-12 Fisher Z-

309 transformation). These validated simulations provided us with specific parameter values at

310 both the global and the local levels associated with healthy control subjects and after stroke.

311

312 *Stroke was associated with reliable changes in global and local parameters*

313 *(Table 3)*

14

314   Although qualitative in nature, the color-coded graphic representation of the variance

315   distribution done as part of the parameter space exploration (Figure 3) provides a glimpse into

316   differences of combined values for the two global parameters: global coupling (x axis) and

317   conduction velocity (y axis) in healthy controls and in stroke subjects, with warm colors

318   representing higher variance. These explorations demonstrated at this early stage of analysis

319   that the range of optimal parameter values (hot colors) in controls had similar topology of the

320   distribution of variance as well as concrete values. In contrast, stroke cases displayed high

321   variations in both topology and values, where although some had similar distribution patterns

322   as the healthy controls, others had scattered, fragmented patterns. Similar observations were

323   found with respect to local parameters.

324   Numerically, differences in parameter values between healthy controls and the stroke

325   cohort are as follows:

326   <u>Global Parameters</u>

327   a.   Conduction velocity: The range of modeled conduction velocities obtained via

328   TVB in healthy controls ranged from 45 to 90 m/s with a mean of 62 ± 10 m/s. In contrast,

329   the conduction velocities in stroke subjects had a range between 12 and 80 m/s with a mean of

330   46 ± 21 m/s. Comparison between the two groups with Wilcoxon rank sum test ($p_c = 0.05$)

331   was marginally significant after correction for multiple comparisons.

332   b.   Global coupling (rescale factor of incoming activity linking global with local

333   dynamics): In healthy controls, the mean was $0.053 ± 0.009$ (range 0.044-0.047) and in cases

334   with stroke the mean was $0.061 ± 0.016$ (range 0.04-0.09). Wilcoxon sum rank test showed

335   this difference was significant after correction for multiple comparisons ($p_c = 0.013$).

15

336   In addition, it is important to note that the trend in all stroke cases where the values

337   were different from those in controls was consistent: that is, it presented always as a decrease

338   in conduction velocities (N = 12) and an increase in global coupling (N = 14). The rest of the

339   stroke cases did not show differences with healthy controls.

340

341   Local parameters derived from the Stefanescu-Jirsa3D model

342   a. K_{12} (coupling of excitatory over inhibitory populations within brain regions):

343   The values of K_{12} in controls had a mean of 0.49 ± 0.338 (range 0.12-0.55) and in stroke the

344   mean was 0.369 ± 0.257 (range 0.1-0.8). Statistical comparison between the two groups

345   resulted in a p_c = 0.17.

346

347   b. K_{21} (coupling of inhibitory over excitatory populations): This variable (control

348   mean = 0.804 ± 0.17, range=0.3-0.9) was significantly reduced in the stroke group (mean =

349   0.674 ± 0.302; range 0.1-0.9; p_c = 0.01).

350

351   c. K_{11} (influence between excitatory populations): The values of K_{11} in controls

352   had a mean of 0.833 ± 0.142 (range 0.6-0.95) and in stroke cases had a mean of 0.613 ± 0.301

353   (range 0.1-0.99). Comparison between the two groups with Wilcoxon sum rank test gave a p_c

354   = 0.1.

355

356   In summary, compared to values in healthy controls, there was a higher global coupling

357   and a decrease of local inhibitory dynamics represented by the local parameter K_{21} along with

358   a trend towards a reduction of conduction velocity.

16

359

Global and local parameters were correlated with clinical phenotype

Multiple linear regression analysis to establish a relationship between modeling parameters and some clinical metrics did not show a correlation. The following clinical elements were considered in this preliminary assessment: stroke phenotype (size, location, time after stroke, side of stroke), depression, patient demographics (age, sex), and severity of impairment.

Next, we assessed the relationship between parameter values with recovery from stroke immediately after therapy and after one year (maintenance) using a multiple linear regression. This analysis showed a negative relationship between K_{12} and Fugl-Meyer scores both post-therapy (t =-2.386; p_d =0.038) and at maintenance one year later (t =-3.824; p_d =0.005). In addition, global coupling had a positive relationship with the Wolf Motor Function Test (t= 2.461; p_d =0.039) at maintenance. Thus, these two parameters derived from modeling based on pre-therapy conditions were related to long-term motor gains rather than the physical features of the stroke or the patient's demographics.

374

375

Statistical Table

	Comparison of Interest	Data Structure	Type of Test	p value
a	Weights of connections: stroke vs. control	Normal	Kolmogorov-Smirnov test	0.42
b	Pearson's correlation coefficients: simulated vs. empirical functional connectivity matrices	Normal after Z-transformation	T test	0.9e-12
c	TVB parameters: stroke vs. control	Control: Non-normal Stroke: Normal	Wilcoxon rank sum test	Conduction Velocity: 0.05 Global Coupling: 0.013 K_{12}: 0.17 K_{21}: 0.01 K_{11}: 0.1
d	Regression: TVB parameters with subject demographics, lesion characteristics and recovery	Normal	Multiple linear regression	Post-Therapy: K_{12} - Fugl-Meyer: 0.038 Maintenance: K_{12} – Fugl-Meyer: 0.005 Global Coupling – WMFT: 0.039

Discussion

377

378   The main result of the study showed that the simulation of BOLD signals using TVB in stroke

379   enables the identification of key changes associated with large-scale neural dynamics in individual

380   patients. Overall, our results showed that, compared to healthy controls, individuals with stroke have

381   a consistent reduction in conduction velocity and a relative increase in local-over-global brain

382   dynamics. Further, the identified parameters were related to functional outcomes such that these

383   parameters predicted long term recovery after therapy. Taken together, these results not only back

384   TVB as an effective tool in identifying dynamic brain changes in stroke spanning multiple scales, but

385   also specifically identify potential predictors of recovery in stroke at the individual level. This study

386   suggests that TVB may be a powerful platform for the application of large-scale modeling in

387   understanding brain mechanisms at an individual subject level.

388

389   *Stroke is related to consistent global and local parameter changes*

390   The successful simulation of empirical rfMRI data in this study facilitated a particularly salient

391   finding; the dynamic model derived from stroke subjects had a significant decrease in the local

392   parameter K_{21} and a consistent global coupling increase, accompanied by a trend in decreased

393   conduction velocity. Two aspects of these results are of special interest: the first relates to the nature

394   of the statistical outcomes and the second to the biological interpretation of these changes.

395   1) Imaging-derived metrics in humans in general have high variance (Mueller et al., 2013);

396   consequently, analytical measures have been developed to minimize it (Fischl et al., 1999). Further,

397   this variance is amplified by stroke (Rehme et al., 2012), and has compelled researchers to stratify

398   patients with precise criteria (Cramer, 2010), resulting in low sample sizes and high inter-study

399   variability. In contrast, even when we used minimal exclusion criteria when selecting participants,

400   changes seen after stroke were highly consistent, where all the cases that had a parameter change with

401   respect to controls had the same directionality and relatively low variance. Given the high level of

402   subject variability (as expected for a cohort including a large range of clinical phenotypes), we find

403   this consistency somewhat surprising. However, we are not suggesting high reliability of our

404   modeling, as the definitive answer will result from expanding the assessment to a larger population

405   where the predictive value of the parameter changes can be formally assessed.

406   2) Stroke survivors exhibited a significant decrease in K_{21}, a parameter at the mesoscopic level

407   that represents the influence of inhibitory on excitatory neuronal populations. A decrease in K_{21} thus

408   indicates local dis-inhibition. These results are highly consistent with existing data on the basic

409   mechanisms of stroke at the cellular level. For example, rodent models of MCA stroke show an

410   imbalance in the density of excitatory and inhibitory receptors in tissue surrounding the lesion

411   (Schiene et al., 1996). Specifically, they suggest a decrease in GABA receptor expression in

412   widespread ipsi-lesional cortical areas and a concomitant increase of N-methyl-D-aspartate (NMDA)

413   receptor expression in the contra-lesional hemisphere.

414   In the context of stroke in humans, hyper-excitability has been described in two experimental

415   paradigms:

416   1) Studies using TMS to test cortical excitability after stroke have shown a decrease in the

417   current needed to elicit motor evoked potentials (MEPs) and an increase in their amplitude (Hallett,

418   2007) along with an expansion in the area producing them (Liepert et al., 2000) suggesting dis-

419   inhibition in motor cortices (Shimizu, 2002). Furthermore, decreasing the hyper-excitability via

420   repetitive low frequency stimulation (Takeuchi et al., 2005) along with a reduction of the TMS

421   stimulation area (Liepert et al., 2000) has been related to motor recovery (Hallett, 2007).

422   2) Increased activity in motor and non-motor regions has been reported in fMRI studies after

423   stroke (Rehme and Grefkes, 2013). Specifically, increased contra-lesional activity has been observed

424   (Grefkes et al., 2008; Ward, 2003; Weiller et al., 1992). Although this has been explained as a

425   recruitment of supplementary areas to assist movement (Rehme and Grefkes, 2013), others have

426   related it to widespread cortical hyper-excitability (Buchkremer-Ratzmann et al., 1996), suggesting

427   long-range cortico-cortical inputs (Logothetis et al., 2001) with increased activation via decreased

428   inhibition (Blicher et al., 2009; Liepert, 2003). Functional recovery has in turn been associated with

429   the degree of recovery of activity in the affected cortical areas (Cramer, 2008).

430   Complementing the above, our results show a correspondence between local and global levels.

431   Indeed, the reduction in local inhibitory influence over excitatory populations was accompanied by an

432   increase in global coupling, reflecting an imbalance after stroke between global and local brain

433   dynamics, favoring the latter. That is, local dynamics exert a stronger influence than global dynamics

434   following stroke. In this case, the imbalance could be exacerbated by the decrease in conduction

435   velocity. Interestingly, this imbalance has also recently been modeled in other brain diseases. For

436   example, early stages of schizophrenia have been associated with a breakdown of local dynamics

437   occurring prior to the disruption of global dynamics occurring later on in disease progression (van den

438   Berg et al., 2012; Rubinov et al., 2009).

439   A particularly interesting finding was the trend associated with a decrease in conduction

440   velocity in individuals with stroke, as it has previously been described through measurements of

441   central motor conduction times (CMCT) via transcranial magnetic stimulation (TMS) in the primary

442   motor cortex. Immediately following stroke, CMCT decreases and correlates with functional measures

443   (Abbruzzese et al., 1991; Pennisi, 2002) tending towards an incomplete normalization over the long-

444   term (Heald et al., 1993). That said, there is a paucity of information on decreased conduction velocity

445   on cortico-cortical connections. The bulk of knowledge derives from studies in rodents showing

446   structural changes to axons and oligodendrocytes in the primary lesion and the ischemic penumbra

447   (Rosenzweig and Carmichael, 2015). And although some degree of re-myelination occurs in the

448   recovery phase, the process is often arrested before completion (Syed et al., 2008). In human autopsy

449   samples, there is an increase in nodal and para-nodal lengths adjacent to lacunar lesions (Hinman et

450   al., 2015), which may lead to decreased conduction velocities (Rasband, 2011). Our results thus

451   provide direction for future animal studies, exemplifying the translational nature of TVB findings.

452   TVB thus appears to be effective at modeling brain activity in healthy brains and those

453   impacted by disease processes, and has the novel capability of studying brain dynamics at multiple

454   scales, including at a level that has thus far only been available via animal models or surrogate

455   neuroimaging markers in humans. Applying this method of modeling, which is tied directly to

456   biological mechanisms, to existing large data sets opens up the possibility to experiment with

457   expanded models of brain states, including a myriad of diseases and their potential treatments.

458

459   *Potential Predictors of Motor Recovery after Stroke*

460   Our results demonstrated that local (K_{12}) and global (global coupling) parameters, derived from

461   pre-therapy conditions, were significantly correlated with motor gains post-therapy and at

462   maintenance. Furthermore, both parameters point in the same direction, as poor recovery was

463   associated with an increase in local excitatory influences and with an emphasis on local dynamics,

464   whereas values closer to controls correlated with better recovery.

465   Interestingly, TVB parameters in stroke did not correlate with severity of disease at the pre-

466   stroke time point, even though the structural connectivity matrix used in the modeling coincided with

467   this time point. In addition, other physical features of the stroke (size, location) or patient

22

468   demographics (sex, age) did not correlate with the modeled parameters. Finally, neither lesion

469   characteristics nor patient demographics correlated with recovery, highlighting the unique predictive

470   potential of these parameters.

471   The question then becomes to what extent these parameter estimates can be used as predictors

472   of recovery at the individual patient level. While a cross-validation approach using the current data set

473   could serve to answer this question, a new and larger stroke cohort is ideal in obtaining estimates of

474   the sensitivity and the specificity of our markers, due to high variance in stroke. However, there is

475   clear value of our observations even with this limitation. At present, biomarkers for stroke recovery

476   have been limited by the use of "substitute or surrogate" measures derived from brain imaging or

477   electrophysiology, mainly due to the inability to measure *in vivo* more ideal basic elements, i.e., at

478   molecular or cellular levels (Burke and Cramer, 2013). Indeed, such elements may be observed more

479   closely in animal models, but are difficult to translate to humans due to the limited homology between

480   species. Specifically, the Stefanescu-Jirsa 3D model used in this study evolved from the mesocopic

481   level Hindmarsh-Rose model. The Hindmarsh-Rose model itself is rooted in the principles of the

482   Hodgkin-Huxley neuron equations, in addition to dynamics based on bursting neurons found in

483   invertebrate circuitry (Hindmarsh and Rose, 1984). Further, the neural behaviors described by the

484   Hindmarsh-Rose model have been biologically verified in other animal models (Gu, 2013; Selverston

485   and Ayers, 2006). Therefore, while any model of the meso-scale does not encompass the complexity

486   of brain processes at the cellular level, there is likely emergence of behavior from the cellular level to

487   the mesoscopic level, exhibiting deterministic behavior that can be modeled and also observed *in vivo*.

488   That is, the transition between the macro- and microscopic level is represented by population

489   dynamics at the mesoscopic level (Mitra, 2014). From this, one could conclude that the path towards

490   basic biomarkers should include the intermediate mesoscopic level. Indeed, TVB allows one not only

491   to estimate parameters at that level but also to link it to the macroscopic global whole-brain level. TVB

492   is not unique in considering biophysical parameters as exemplified by inference models based on

493   DCM (Moran et al., 2011). Basically, there are no conceptual differences in the inferential goals

494   between TVB and DCM but they do differ in the detailed mechanics. For example, whereas TVB

495   develops the model at the level of large-scale networks, DCM focuses on portions of these networks.

496   Second, and perhaps the key contrast is that while DCM fits the parameter of the model but does not

497   generate data, TVB uses the model to generate data, making these two approaches highly

498   complementary.

499   An interesting and unique aspect of TVB is its highly individualized approach, as parameter

500   estimates are derived from individualized structural connectivity matrices obtained from each subject,

501   and hence, it can provide the first step to customize *individual* therapeutic interventions. For example,

502   our ongoing work is beginning to test potential "virtual interventions" by modifying specific

503   parameters changed after stroke and determining the degree of restoration of brain dynamics on each

504   stroke patient.

505   A second ability of this modeling approach is to use the model of an individual patient's brain

506   connectivity that can be objectively measured and evaluated as an indicator of normal biological

507   processes (such as resting state activity, rsfMRI), pathogenic processes, or pharmacologic responses

508   to therapeutic intervention (Group, 2001). Dynamics of rsfMRI are highly non-stationary (Allen et al.,

509   2014) and existing metrics, including the direct correlation between functional and structural

510   connectivity, are so far incapable of addressing this issue satisfactorily (Goni, 2013). A number of

511   studies have therefore used generative modeling to parse the relationship between structural and

512   functional connectivity. A recent study (Andersen et al., 2014) demonstrated that the fusion of TVB-

513   like network modeling with structural neuroimaging explains the non-stationary dynamics observed

514   in rsfMRI. Thus we propose a conceptual paradigm shift, in which the dynamic model shifts the non-

515   stationary functional data from imaging at the mesoscopic scale to a more deterministic set of

516   coefficients in a brain model. In other words, complex dynamics cannot be captured by stationary

517   imaging analyses, but can be generated by a data-constrained mechanistic model of brain circuit

518   dynamics, as seen in the generative modeling approach detailed in stroke (Brodersen et al., 2011).

519   Thus, the mathematical model could be seen as a compact generator of dynamics-based biomarkers,

520   or even as the biomarker itself. The primary benefit, as we demonstrated here, is that it becomes easier

521   to understand disease mechanisms by evaluating the coefficients of the model.

522   Of note, the approach used in this study to validate the simulated time series was to compare

523   frequency, amplitude and phase of the simulated and empirical signals. After the refinement of the

524   TVB models, future studies will incorporate a larger variety of multi-dimensional analyses,

525   particularly with respect to temporal variability in resting state signals. Furthermore, the current study

526   determined optimal values of local parameters applied to all brain regions. Future studies will focus

527   on local parameters for subsets of brain regions, e.g., changing parameters of nodes within and/or

528   around a stroke lesion to determine how this impacts the resultant simulated brain activity. We also

529   note that the translational power of our findings depends upon the reproducibility of parameters for a

530   given brain state, the answer for which will emerge with expanded application of TVB to other cohorts.

531   The results from this study thus confirm that TVB allows the assessment of biophysical variables

532   previously unattainable in human studies. This method provides a potentially important and novel

533   application of large-scale modeling, in which we can probe brain dynamics and biomarkers on an

534   individual level. Therefore, The Virtual Brain has the potential to become an important step towards

535   the development of individualized medicine in stroke.

536

537
538

539 **References**
540

541 Abbruzzese, G., Morena, M., Dall'Agata, D., Abbruzzese, M., and Favale, E. (1991). Motor

542 evoked potentials (MEPs) in lacunar syndromes. Electroencephalogr. Clin. Neurophysiol.

543 Potentials Sect. *81*, 202–208.

544 Allen, E.A., Damaraju, E., Plis, S.M., Erhardt, E.B., Eichele, T., and Calhoun, V.D. (2014).

545 Tracking whole-brain connectivity dynamics in the resting state. Cereb. Cortex *24*, 663–676.

546 Andersen, K.W., Madsen, K.H., Siebner, H.R., Schmidt, M.N., Mørup, M., and Hansen, L.K.

547 (2014). Non-parametric Bayesian graph models reveal community structure in resting state

548 fMRI. Neuroimage *100*, 301–315.

549 Avants, B.B., Tustison, N.J., Song, G., Cook, P.A., Klein, A., and Gee, J.C. (2011). A

550 reproducible evaluation of ANTs similarity metric performance in brain image registration.

551 Neuroimage *54*, 2033–2044.

552 van den Berg, D., Gong, P., Breakspear, M., and van Leeuwen, C. (2012). Fragmentation:

553 loss of global coherence or breakdown of modularity in functional brain architecture? Front.

554 Syst. Neurosci. *6*, 20.

555 Blicher, J.U., Jakobsen, J., Andersen, G., and Nielsen, J.F. (2009). Cortical excitability in

556 chronic stroke and modulation by training: a TMS study. Neurorehabil. Neural Repair *23*,

557 486–493.

558 Boynton, G.M., Engel, S.A., Glover, G.H., and Heeger, D.J. (1996). Linear systems analysis

559 of functional magnetic resonance imaging in human V1. J. Neurosci. *16*, 4207–4221.

560 Breakspear, M., and Jirsa, V.K. (2007). Neuronal Dynamics and Brain Connectivity. In

561 Handbook of Brain Connectivity, V.K. Jirsa, and A.R. Mcintosh, eds. (Springer), pp. 3–64.

562   Brodersen, K.H., Schofield, T.M., Leff, A.P., Ong, C.S., Lomakina, E.I., Buhmann, J.M., and

563   Stephan, K.E. (2011). Generative embedding for model-based classification of fMRI data.

564   PLoS Comput. Biol. *7*, e1002079.

565   Buchkremer-Ratzmann, I., August, M., Hagemann, G., and Witte, O.W. (1996).

566   Electrophysiological transcortical diaschisis after cortical photothrombosis in rat brain.

567   Stroke. *27*, 1105–1109; discussion 1109–1111.

568   Burke, E., and Cramer, S.C. (2013). Biomarkers and predictors of restorative therapy effects

569   after stroke. Curr. Neurol. Neurosci. Rep. *13*, 329.

570   Carmichael, S.T. (2012). Brain excitability in stroke: the yin and yang of stroke progression.

571   Arch. Neurol. *69*, 161–167.

572   Cox, R.W. (1996). AFNI: software for analysis and visualization of functional magnetic

573   resonance neuroimages. Comput. Biomed. Res. *29*, 162–173.

574   Cox, R.W., and Jesmanowicz, A. (1999). Real-time 3D image registration for functional

575   MRI. Magn. Reson. Med. *42*, 1014–1018.

576   Cramer, S.C. (2008). Repairing the human brain after stroke: I. Mechanisms of spontaneous

577   recovery. Ann. Neurol. *63*, 272–287.

578   Cramer, S.C. (2010). Stratifying patients with stroke in trials that target brain repair. Stroke.

579   *41*, S114–S116.

580   Deco, G., Senden, M., and Jirsa, V. (2012). How anatomy shapes dynamics: a semi-

581   analytical study of the brain at rest by a simple spin model. Front. Comput. Neurosci. *6*, 68.

582   Van Essen, D.C. (2004). Surface-based approaches to spatial localization and registration in

583   primate cerebral cortex. Neuroimage *23 Suppl 1*, S97–S107.

584   Van Essen, D.C. (2005). A Population-Average, Landmark- and Surface-based (PALS) atlas

585   of human cerebral cortex. Neuroimage *28*, 635–662.

586   Van Essen, D.C., and Dierker, D.L. (2007). Surface-based and probabilistic atlases of

587   primate cerebral cortex. Neuron *56*, 209–225.

588   Fischl, B., Sereno, M.I., Tootell, R.B., and Dale, A.M. (1999). High-resolution intersubject

589   averaging and a coordinate system for the cortical surface. Hum. Brain Mapp. *8*, 272–284.

590   Go, A.S., Mozaffarian, D., Roger, V.L., Benjamin, E.J., Berry, J.D., Blaha, M.J., Dai, S.,

591   Ford, E.S., Fox, C.S., Franco, S., et al. (2014). Heart disease and stroke statistics--2014

592   update: a report from the American Heart Association. Circulation *129*, e28–e292.

593   Goni, J. (2013). Resting-brain functional connectivity predicted by analytic measures of

594   network communication.

595   Grefkes, C., Nowak, D.A., Eickhoff, S.B., Dafotakis, M., Küst, J., Karbe, H., and Fink, G.R.

596   (2008). Cortical connectivity after subcortical stroke assessed with functional magnetic

597   resonance imaging. Ann. Neurol. *63*, 236–246.

598   Group, B.D.W. (2001). Biomarkers and surrogate endpoints: preferred definitions and

599   conceptual framework. Clin. Pharmacol. Ther. *69*, 89–95.

600   Gu, H. (2013). Biological experimental observations of an unnoticed chaos as simulated by

601   the Hindmarsh-Rose model. PLoS One *8*, e81759.

602   Hallett, M. (2007). Transcranial magnetic stimulation: a primer. Neuron *55*, 187–199.

603   Heald, A., Bates, D., Cartlidge, N.E., French, J.M., and Miller, S. (1993). Longitudinal study

604   of central motor conduction time following stroke. 1. Natural history of central motor

605   conduction. Brain *116 (Pt 6*, 1355–1370.

606 Hindmarsh, J.L., and Rose, R.M. (1984). A Model of Neuronal Bursting Using Three

607 Coupled First Order Differential Equations. Proc. R. Soc. B Biol. Sci. *221*, 87–102.

608 Hinman, J.D., Lee, M.D., Tung, S., Vinters, H. V, and Carmichael, S.T. (2015). Molecular

609 disorganization of axons adjacent to human lacunar infarcts. Brain *138*, 736–745.

610 Hutchison, R.M., Womelsdorf, T., Allen, E.A., Bandettini, P.A., Calhoun, V.D., Corbetta,

611 M., Della Penna, S., Duyn, J.H., Glover, G.H., Gonzalez-Castillo, J., et al. (2013). Dynamic

612 functional connectivity: promise, issues, and interpretations. Neuroimage *80*, 360–378.

613 Jirsa, V.K., and Stefanescu, R.A. (2011). Neural population modes capture biologically

614 realistic large scale network dynamics. Bull. Math. Biol. *73*, 325–343.

615 Johnstone, T., Ores Walsh, K.S., Greischar, L.L., Alexander, A.L., Fox, A.S., Davidson, R.J.,

616 and Oakes, T.R. (2006). Motion correction and the use of motion covariates in multiple-

617 subject fMRI analysis. Hum. Brain Mapp. *27*, 779–788.

618 Leemans, A., and Jones, D.K. (2009). The B-matrix must be rotated when correcting for

619 subject motion in DTI data. Magn. Reson. Med. *61*, 1336–1349.

620 Liepert, J. (2003). TMS in stroke. Suppl. Clin. Neurophysiol. *56*, 368–380.

621 Liepert, J., Graef, S., Uhde, I., Leidner, O., and Weiller, C. (2000). Training-induced changes

622 of motor cortex representations in stroke patients. Acta Neurol. Scand. *101*, 321–326.

623 Logothetis, N.K., Pauls, J., Augath, M., Trinath, T., and Oeltermann, a (2001).

624 Neurophysiological investigation of the basis of the fMRI signal. Nature *412*, 150–157.

625 Lund, T.E., Madsen, K.H., Sidaros, K., Luo, W.-L., and Nichols, T.E. (2006). Non-white

626 noise in fMRI: does modelling have an impact? Neuroimage *29*, 54–66.

627 Mannella, R. (2002). Integration of stochastic differential equations on a computer.

628   Mitra, P.P. (2014). The Circuit Architecture of Whole Brains at the Mesoscopic Scale.

629   Neuron *83*, 1273–1283.

630   Moran, R.J., Symmonds, M., Stephan, K.E., Friston, K.J., and Dolan, R.J. (2011). An in vivo

631   assay of synaptic function mediating human cognition. Curr. Biol. *21*, 1320–1325.

632   Mueller, S., Wang, D., Fox, M.D., Yeo, B.T.T., Sepulcre, J., Sabuncu, M.R., Shafee, R., Lu,

633   J., and Liu, H. (2013). Individual variability in functional connectivity architecture of the

634   human brain. Neuron *77*, 586–595.

635   Nudo, R.J. (2013). Recovery after brain injury: mechanisms and principles. Front. Hum.

636   Neurosci. *7*, 887.

637   Pennisi, G. (2002). Transcranial magnetic stimulation after pure motor stroke. Clin.

638   Neurophysiol. *113*, 1536–1543.

639   Rasband, M.N. (2011). Composition, assembly, and maintenance of excitable membrane

640   domains in myelinated axons. Semin. Cell Dev. Biol. *22*, 178–184.

641   Rehme, A.K., and Grefkes, C. (2013). Cerebral network disorders after stroke: evidence from

642   imaging-based connectivity analyses of active and resting brain states in humans. J. Physiol.

643   *591*, 17–31.

644   Rehme, A.K., Eickhoff, S.B., Rottschy, C., Fink, G.R., and Grefkes, C. (2012). Activation

645   likelihood estimation meta-analysis of motor-related neural activity after stroke. Neuroimage

646   *59*, 2771–2782.

647   Reiss, A.P., Wolf, S.L., Hammel, E.A., McLeod, E.L., and Williams, E.A. (2012).

648   Constraint-Induced Movement Therapy (CIMT): Current Perspectives and Future Directions.

649   Stroke Res. Treat. *2012*, 159391.

650　Ritter, P., Schirner, M., McIntosh, A.R., and Jirsa, V. (2013). The Virtual Brain Integrates

651　Computational Modelling and Multimodal Neuroimaging. Brain Connect. *49*, 1–65.

652　Rosenzweig, S., and Carmichael, S.T. (2015). The axon-glia unit in white matter stroke:

653　Mechanisms of damage and recovery. Brain Res. *1623*, 123–134.

654　Roy, D., Sigala, R., Breakspear, M., McIntosh, A.R., Jirsa, V.K., Deco, G., and Ritter, P.

655　(2014). Using the virtual brain to reveal the role of oscillations and plasticity in shaping

656　brain's dynamical landscape. Brain Connect. *4*, 791–811.

657　Rubinov, M., Sporns, O., van Leeuwen, C., and Breakspear, M. (2009). Symbiotic

658　relationship between brain structure and dynamics. BMC Neurosci. *10*, 55.

659　Sanz Leon, P., Knock, S. a, Woodman, M.M., Domide, L., Mersmann, J., McIntosh, A.R.,

660　and Jirsa, V. (2013). The Virtual Brain: a simulator of primate brain network dynamics.

661　Front. Neuroinform. *7*, 10.

662　Sanz-Leon, P., Knock, S.A., Spiegler, A., and Jirsa, V.K. (2015). Mathematical framework

663　for large-scale brain network modelling in The Virtual Brain. Neuroimage *111*, 385–430.

664　Schiene, K., Bruehl, C., Zilles, K., Qü, M., Hagemann, G., Kraemer, M., and Witte, O.W.

665　(1996). Neuronal hyperexcitability and reduction of GABAA-receptor expression in the

666　surround of cerebral photothrombosis. J. Cereb. Blood Flow Metab. *16*, 906–914.

667　Selverston, A.I., and Ayers, J. (2006). Oscillations and oscillatory behavior in small neural

668　circuits. Biol. Cybern. *95*, 537–554.

669　Shimizu, T. (2002). Motor cortical disinhibition in the unaffected hemisphere after unilateral

670　cortical stroke. Brain *125*, 1896–1907.

671　Smith, S.M. (2002). Fast robust automated brain extraction. Hum. Brain Mapp. *17*, 143–155.

672   Solodkin, A., Hasson, U., Siugzdaite, R., Schiel, M., Chen, E.E., Kotter, R., and Small, S.L.

673   (2010). Virtual brain transplantation (VBT): a method for accurate image registration and

674   parcellation in large cortical stroke. Arch. Ital. Biol. *148*, 219–241.

675   Stefanescu, R. a, and Jirsa, V.K. (2008). A low dimensional description of globally coupled

676   heterogeneous neural networks of excitatory and inhibitory neurons. PLoS Comput. Biol. *4*,

677   e1000219.

678   Syed, Y.A., Baer, A.S., Lubec, G., Hoeger, H., Widhalm, G., and Kotter, M.R. (2008).

679   Inhibition of oligodendrocyte precursor cell differentiation by myelin-associated proteins.

680   Neurosurg. Focus *24*, E5.

681   Takeuchi, N., Chuma, T., Matsuo, Y., Watanabe, I., and Ikoma, K. (2005). Repetitive

682   transcranial magnetic stimulation of contralesional primary motor cortex improves hand

683   function after stroke. Stroke. *36*, 2681–2686.

684   Ward, N.S. (2003). Neural correlates of outcome after stroke: a cross-sectional fMRI study.

685   Brain *126*, 1430–1448.

686   Weiller, C., Chollet, F., Friston, K.J., Wise, R.J., and Frackowiak, R.S. (1992). Functional

687   reorganization of the brain in recovery from striatocapsular infarction in man. Ann. Neurol.

688   *31*, 463–472.

689   Zalesky, A., and Fornito, A. (2009). A DTI-derived measure of cortico-cortical connectivity.

690   IEEE Trans. Med. Imaging *28*, 1023–1036.

691   Zhang, Y., Brady, M., and Smith, S. (2001). Segmentation of brain MR images through a

692   hidden Markov random field model and the expectation-maximization algorithm. IEEE

693   Trans. Med. Imaging *20*, 45–57.

694

695

Legends to Figures

696
697

698   *Figure 1: Simulation workflow in TVB.*

699   Graphic representation depicting the sequential steps of TVB modeling. (**A**) Empirical inputs

700 (structural connectome) are generated from DTI tractography based on T1-w brain parcellation. (**B**)

701 Subsequent parameter exploration at the global and local levels (w = weights, cv = conduction

702 velocity, c= global coupling). (**C**) Once parameter values are obtained, the BOLD signal is simulated.

703 (**D**) The efficacy of the simulation is calculated by correlating it to the empirical signals.

704

705   *Figure 2: Equations of the Stefanescu-Jirsa 3D model.*

706   (**A**) Evolution equation implemented in The Virtual Brain to simulate brain activity. The mean

707 field potential $x_i(t)$ of a region i at time t is dependent on the local dynamics $f(x_i(t))$ provided by the

708 Stefanescu-Jirsa-3D model, the long-range structural connectivity w, which links regions i and j and

709 is provided by the input of individual structural connectivity matrices (weights), and noise $\eta(t)$). Time

710 delays (Δt) are distance dependent and are provided by the structural connectivity matrices (lengths).

711 All mathematical details of the model and its numerical implementation are provided in (Sanz-Leon

712 et al. (2015, in press)). (**B**) Equations comprising Stefanescu-Jirsa 3D. The first 3 (ξ, η, τ) equations

713 represent the excitatory sub-population of neurons within a local region, while the last 3 equations (

714 α, β, γ) represent the inhibitory sub-population of neurons in that region. IE and II denote the input

715 current to the excitatory and inhibitory populations of each node, respectively. The first of each of the

716 two sets of equations accounts for neuron potentials. The second and third equations account for the

717 transport of ions across the membrane through ion channels. Note that the dynamics of these

718 populations are dependent on the interactions between inhibitory and excitatory influences (K_{12}, K_{21},

719 K_{11}).

35

720

721   ***Figure 3:** Examples of global parameter space exploration in healthy controls and stroke.* Two

722   examples of heat graphs of global variance (mean variance of the time series across all regions) used

723   to narrow down the range of parameter values more suitable for modeling in (**A**) a healthy control and

724   (**B**) a stroke case. Global coupling is shown on the x-axis and conduction velocity (m/s) on the y-axis.

725   Colors indicate degree of global variance with hotter colors indicating higher values. White arrows

726   show the range of values considered for global coupling limited by bifurcation points (yellow). Black

727   arrows point to the range in conduction velocity considered in each case. Note the higher range of

728   values associated with global coupling and lower for conduction velocity in the stroke case.

729

730   ***Figure 4:** Weights of structural connections in stroke and healthy controls.*

731   (**A**) Structural connectivity matrices in a healthy control (left) and one individual with stroke

732   (right). Dark blue denotes absence of connections while hotter colors indicate stronger weights. (**B**)

733   Frequency distribution of weight of connections in healthy controls (orange bars) and stroke (blue

734   bars).

735

736   ***Figure 5:** Comparison of simulated and empirical BOLD signals.*

737   (**A**) Amplitude: Example of a raw simulated (left) and empirical (right) time series (TS).

738   Amplitudes are indicated by the maxima and minima of the time series. (**B**) Frequency: Frequency

739   distribution graphs (FFT) of the simulated (left) and empirical (right) time series. Note that both

740   empirical and simulated signals have the same range, profiles, and peaks. (**C**) Phase: Functional

741   connectivity (FC) matrix based on simulated time series (left) and the empirical group matrix (right).

742

36

743   ***Figure 6:*** *Correlation between modeling parameters and post-therapy motor outcomes.*

744   Scatterplots showing correlation between TVB modeling parameters (x-axis) and post-therapy

745 motor outcomes (y-axis). Clear relationships were found between (**A**) k12 and Fugl-Meyer (Post-

746 therapy), (**B**) k12 and Fugl-Meyer (Maintenance), and (**C**) Global coupling and WMFT

747 (Maintenance).

748

749

750 **Tables**

Subject	Age	Sex	Handedness	Affected Hemisphere	Affected Hand	Stroke Location	Stroke Volume (mm^3)
1	41	F	Right	Right	ND	Cort	22495.0
2	54	F	Right	Left	D	Cort/subcort	49078.0
3	57	M	Right	Left	D	Cort/subcort	17411.0
4	57	M	Right	Left	D	Cort/subcort	38703.0
5	54	F	Right	Left	D	Subcort	27677.0
6	50	M	Right	Right	ND	Subcort	3570.0
7	23	M	Right	Left	D	Subcort	560.0
8	55	F	Right	Right	ND	Cort	6781.0
9	68	M	Right	Left	D	Subcort	1988.3
10	56	F	Right	Left	D	Subcort	6239.7
11	46	M	Right	Left	D	Subcort	325.0
12	56	F	Left	Right	D	Cort/subcort	60669.0
13	37	M	Right	Left	D	Cort/subcort	83406.2
14	62	M	Right	Left	D	Subcort	22154.8
15	57	M	Right	Right	ND	Cort/subcort	25392.0
16	66	M	Right	Left	ND	Cort/subcort	19927.0
17	61	M	Right	Left	D	Subcort	978.0
18	74	M	Right	Left	D	Cort/subcort	63642.0
19	67	F	Right	Right	ND	Subcort	588.0
20	74	F	Right	Left	D	Cort/subcort	44892.0

751

752   **Table 1:** Demographics and stroke characteristics of the stroke cohort.   D = dominant

753   hemisphere; ND = non-dominant hemisphere, Cort = cortical, Subcort = subcortical.

754

755

Parameter	Value	Description
a, b, c, d	1, 3, 1, 5	Constants affecting faster ion channels
r	0.006	Constant affecting slower ion channels
s	4	Bursting strength of model
μ and σ	2.2, 0.3	Mean and dispersion of input current in each node
X_0	-1.6	Leftmost equilibrium point of X
IE, II	Derived from μ and σ	Models excitability of each node and mode (IE for excitatory input, II for inhibitory input)
Global Coupling	0.01-1.0	Coupling scaling factor for connections between nodes
Conduction velocity	10-100	Scales delay for defined internode distances
β, γ	4, 5	Corresponding values for IPs
K_{12}, K_{21}, K_{11}	0.01-1.0	Models coupling between excitatory and inhibitory populations within nodes

756

757   **Table 2:** State variables and parameters of the Stefanescu-Jirsa 3D model and
758 corresponding range of values used in the present study. Values used for the simulation
759 included global coupling, conduction velocity, and K_{12}, K_{21}, and K_{11} optimized via parameter
760 space explorations. Default values were used for all other variables.

761

762

763

764

765

39

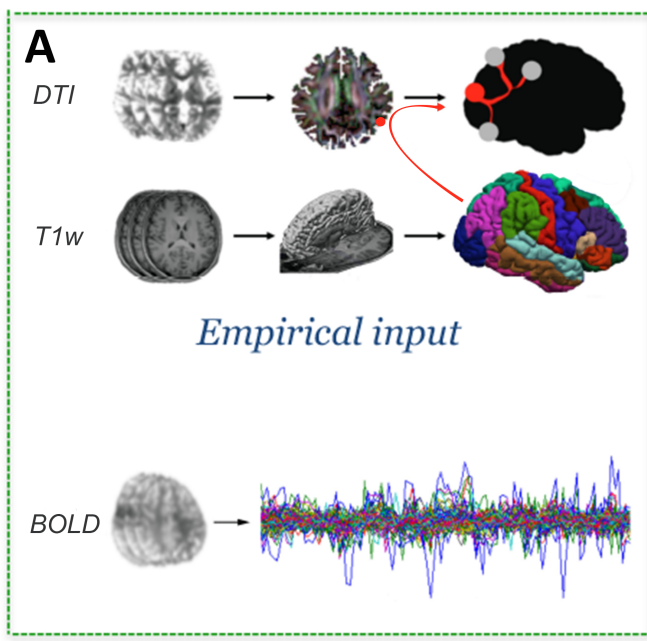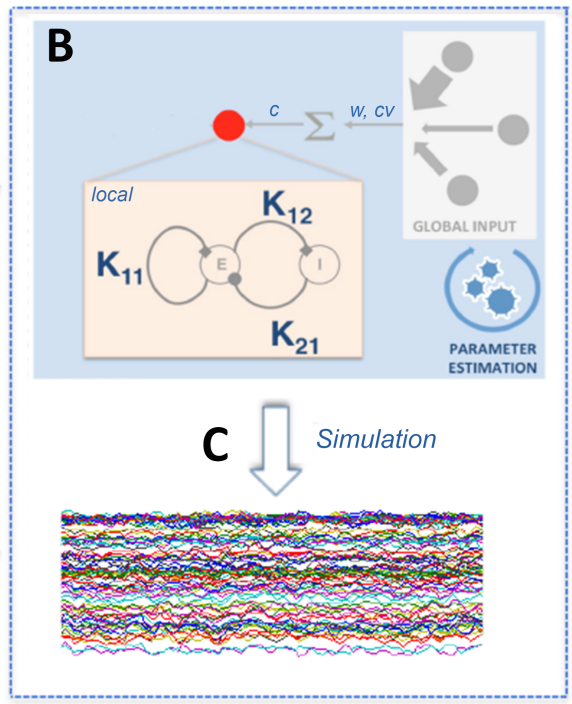| Group	Variable	Range	Mean	SD	Wilcoxon Rank Sum (p)
Control	Global Variables:				
	Global Coupling	0.044-0.047	0.053	0.009	
	Conduction Velocity	45-90	61.9	9.9	
	Model Variables:				
	K_{12}	0.12-0.55	0.49	0.338	
	K_{21}	0.3-0.9	0.804	0.17	
	K_{11}	0.6-0.95	0.833	0.142	
Stroke	Global Variables:				
	Global Coupling	0.04-0.09	0.061	0.016	0.013
	Conduction Velocity	12-80	46	21	0.05
	Model Variables:				
	K_{12}	0.1-0.8	0.369	0.257	0.17
	K_{21}	0.1-0.9	0.674	0.302	0.01
	K_{11}	0.1-0.99	0.613	0.301	0.1

766

767 **Table 3:** Summary of long-range and local parameters used in TVB to simulate BOLD time series

768 in healthy controls and individuals with stroke. SD = standard deviation. p = probability resulting from

769 the Wilcoxon sum rank test comparing parameter values between the two groups.

A

Mean Field Potential   Time Delay   Noise

$$\dot{x}_i(t) = f\big(x_i(t)\big) + c \sum_{j=1}^{N} w_{ij} x_j\big(t - \Delta t_{ij}\big) + \eta(t)$$

Stefanescu-Jirsa 3D   Long-Range Structural Connectivity

B

$$\dot{\xi}_i = \eta_i - a_i \xi_i^3 + b_i \xi_i^2 - \tau_i + K_{11}\left[\sum_{k=1}^{3} A_{ik} \xi_k - \xi_i\right] - K_{12}\left[\sum_{k=1}^{3} B_{ik} \alpha_k - \xi_i\right] + IE_i$$

$$\dot{\eta}_i = c_i - d_i \xi_i^2 - \eta_i$$

$$\dot{\tau}_i = rs\xi_i - r\tau_i - m_i$$

$$\dot{\alpha}_i = \beta_i - e_i \alpha_i^3 + f_i \alpha_i^2 - \gamma_i + K_{21}\left[\sum_{k=1}^{3} C_{ik} \xi_k - \alpha_i\right] + II_i$$

$$\dot{\beta}_i = h_i - p_i \alpha_i^2 - \beta_i$$

$$\dot{\gamma}_i = rs\alpha_i - r\gamma_i - n_i$$

Simulated

Empirical

A.

B.

C.

Post-Therapy

Maintenance

A — Motor Assessment: Fugl-Meyer vs k12

B — Motor Assessment: Fugl-Meyer vs k12

C — Motor Assessment: WMFT (s) vs Global Coupling